Adaptive and active X-ray optics

© *V.V. Lider*

Institute of Crystallography named after A.V. Shubnikov FSRC „Crystallography and Photonics" RAS,
119333 Moscow, Russia

e-mail: vallider@yandex.ru

This review describes the principles and capabilities of X-ray adaptive and active optics. The main executive mechanisms of bending mirrors used at synchrotron radiation sources and in X-ray telescopes are considered. Particular attention is paid to wavefront metrology using Shack−Hartmann sensors, as well as sensors based on grating interferometers, X-ray speckle and ptychography.

Keywords: X-rays, adaptive optics, active optics, bimorph mirror, wavefront metrology.

1. Introduction

Active and adaptive optics have been used for several decades in many scientific disciplines, including astronomy, laser physics, X-ray microscopy, and X-ray diffractometry. Active and adaptive optics supplement each other — they are combined by a common idea — elimination of non-regular distortions resulting from the distribution of irradiation in heterogeneous medium with the use of controlled optical components. Unlike passive optics with fixed, pre-polished surface profiles, active and adaptive optics can be deformed to fit different experimental problems. From a semantic point of view, the use of these terms is somewhat arbitrary and has led and still leads to some confusion.

The concept of adaptive optics was first introduced by Kh.W. Babcock [1] and V.P. Linnik [2] in connection with the problem of improving the quality of images of celestial objects obtained by Earth-based telescopes. For ground-based telescopes, it has been proposed [3] to use the term „adaptive" to describe wavefront distortion correction by atmospheric turbulence and the term „active" to describe how wavefront distortion caused by mechanical, thermal and optical effects in the telescope itself can be controlled.

However, the X-ray telescope (like other X-ray instruments) does not face the problem of atmospheric turbulence. Therefore, here we will understand by the adaptive optics the one that compensates wavefront distortions created by downward (preliminary) and upward optics (for example, mirrors, monochromators, slits and apertures in the case of experimental stations on synchrotron radiation (SR) beam). Optics correcting wavefront distortions caused, for example, by defects in the shape of the reflecting mirror surface will be called active.

The phase change of $\Delta\varphi$ in reflection from a protrusion on the surface of the mirror with a height h is [5]

$$\Delta\varphi = (4\pi h/\lambda)\sin\theta, \qquad (1)$$

where θ — slip angle, λ — radiation wavelength. Therefore, defects of X-ray-optical elements can be analyzed by their influence on the wavefront of radiation. Therefore, the review will consider not only X-ray adaptive and active optics, but also metrology *in situ* to characterize and optimize optical elements.

2. Executive mechanisms

An X-ray microbeam — is an effective tool for characterizing a substance with wide possibilities of use: from materials science and biomedicine to environmental science and astrophysics [6]. Any kind of focusing when reflecting X-rays can be achieved only with a curved reflective surface. The full external reflection mirror focusing system is one of the most promising methods for producing nano-focused X-ray radiation due to its high efficiency and energy-adjustable focus.

Since full-external reflection optics is achromatic over a large energy range and retains a reflectivity close to one, it should be recognized as the most promising way to focus the X-ray under the condition of a small sliding angle θ ($\theta \leq \theta_c$). The value of limiting angle θ_c (mrad) is given by the approximate formula:

$$\theta_c = (2\delta)^{1/2} \approx 2.34\lambda(Z\rho/A)^{1/2}, \qquad (2)$$

where δ — decrement of the refractive ratio n ($n = 1-\delta$), ρ (g/cm^3) — material density, Z and A — its atomic number and weight, respectively, λ (Å) — X-ray wavelength.

High-quality optical surface and good bending characteristics are necessary to ensure accurate X-ray beam focus. High-quality optical surface can be obtained by polishing methods such as ion bundle polishing [7] and elastic emission treatment (EEM) [8]. Active and adaptive optics can provide the necessary good bending characteristics. The main bending mechanisms should be considered mechan-

ical, electrostatic, piezoelectric, electromagnetic, thermal. Each of them has its advantages and limitations [9].

2.1. Mechanical bending devices

The design principle underlying bending optics is based on the simple theory of beam elasticity. It is well known that a flat beam of uniform cross-section can be bent by applying two independent bending moments to its ends. Typically, an elliptical or ellipsoid surface of a mirror or its close approximation is used to avoid or minimize aberration. For the required aspherical (elliptical) profile, the radius of curvature $R(x)$ of the curved mirror varies in length depending on the coordinate x. Using mechanical beam theory, the local curvature $1/R(x)$ can be calculated as follows [10,11]:

$$1/R(x) = \partial^2 u / \partial x^2 = M(x)/EI(x), \qquad (3)$$

$$I(x) = W(x)t^3(x)/12, \qquad (4)$$

where u — vertical mirror offset, x — mirror point coordinate, $M(x)$ — local bending moments, E and $I(x)$) — mirror elastic modulus and local inertia moment, $W(x)$ and $t(x)$ — its local width and thickness respectively. For the rectangular prism $I(x)$ is constant. To obtain the shape of an elliptical cylinder, the usual practice is the use of a trapezoid profile, i.e., a linear variation of the width of the substrate $W(x)$ along the mirror. To correct the shape errors, the profiles of more complex width should be used (quadratic and above) [12]. For the ease of manufacture, the thickness of the substrate $t(x)$ remains constant over the length of the mirror. This analytical approach is valid if one assumes that only bending moments are applied to the mirror. The use of an iterative modeling procedure [13] allows optimizing the mirror width profile for a particular optical configuration [14]. Mechanically curved X-ray mirrors are used successfully, in particular, at many synchrotron experimental stations [15–18].

Although mechanical bending optical systems successfully focus X-ray to sub-micron dimensions, it should be noted that they have some practical limitations [10]. First, they are sensitive to the adjustment of the bending device. Second, they are bulky. Finally, in practice, mechanically curved mirrors cannot correspond to the exact shapes providing focal spots of nanometer size [19,20].

2.2. Electrostatic actuators

Electrostatic actuators have become more widespread due to their high compatibility with microtechnology processes, low power consumption, simple design and short response time.

The basic principle of an electrostatic deformable mirror (DM) is the use of an attraction force between two parallel plates when applying different voltage to each plate. The electrostatic drive can only have pulling (attractive) force. The electrostatic force created by applying the voltage
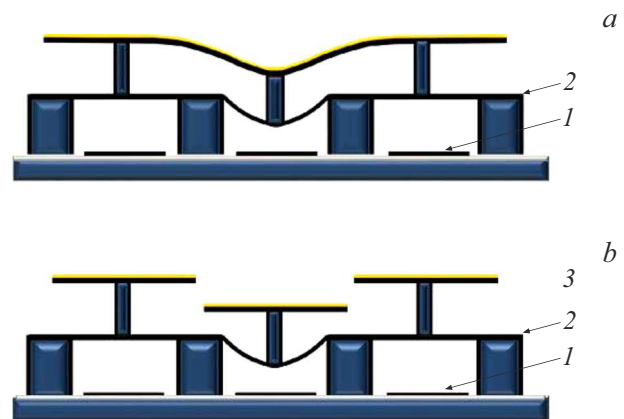

Figure 1. Construction of continuous (a) and segmented (b) electrostatic actuators *1* — lower electrode, *2* — upper electrode of the executing mechanism, *3* — mirror.

between the 1st layer (bottom electrode) and 2nd layer (electrode of the executing mechanism) pulls the membrane of the executing mechanism (Fig. 1). As a result, the front surface of the mirror (3rd layer) is deformed according to the actuator movement.

Deformable mirrors can be divided into segmented and continuous mirrors depending on their design. The segmented DM (Fig. 1, b) consists of a set of compact mirror segments and their movements are controlled by corresponding drives. Thus, the correction of distortion of the mirror surface shape can be achieved at the expense of individual contribution of each of its segments. Segmented DM have several advantages, including easy segment replacement, lack of mechanical cross-linking between mirror segments, and unlimited aperture by adding additional segments. However, heterogeneity (spacing) between segments may inadvertently and uncontrollably dissipate the incident radiation. The continuous surface mirror (Fig. 1, a) is created on the basis of a single drive with a set of actuators. They give a smooth deformation because they have no gaps. However, the production of long deformable embedded piezo-mirrors is difficult, as they require long piezoelectric devices [21]. Deformable mirrors made using polycrystalline silicon are extremely light and compact [22], consume very little energy and scale to masses of thousands of actuators [23]. For example, the DM model with the array of executing mechanisms 64×64 is capable of creating a stroke $3.5 \, \mu m$ with a pitch of executing elements $300 \sim 450 \, \mu m$ with a thin silicon membrane [24]. However, such a DM suffers from high operating voltage ($> 200 \, V$) at a strain of $\sim 5 \, \mu m$ due to the small surface area of the electrode and the rigid mirror membrane. Moreover, the manufacturing process is complicated by defects in the material, which are difficult to repair. Low production is a serious problem. Further, there is a well-known instability caused by the electrostatic force between two parallel plates, which occurs at a distance of $2/3$ of the opening gap. This is known as the static retraction
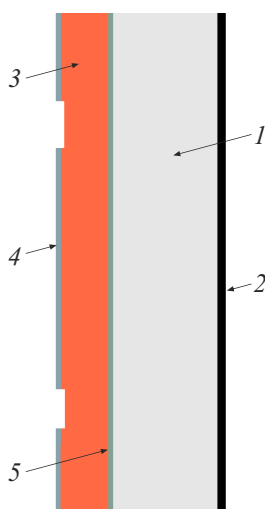
Figure 2. Design of solid shear monomorphic mirror: *1* — mirror substrate, *2* — reflective layer, *3* — piezoceramic layer, *4* — independent electrode system, *5* — grounded electrode [27].

Figure 3. The actuator design using micron-sized fibers and counter-pin surface electrodes: *1* — system of parallel piezoelectric fibers, *2* — polymer matrix, *3* — counter-pin electrodes [47].

state [25]. Therefore, the gap between the two plates must be large enough to increase the control voltage [21].

2.3. Piezoelectric actuators

A piezoelectric actuator (piezoactuator) — the device using piezoceramics ability to expand under the action of the electrostatic field to generate force and move in the micrometer range [26]. Piezoelectric actuators use the reverse piezoelectric effect to convert electrical energy into mechanical energy or mechanical motion. Thanks to the advantages of simple design, light weight and quick response, piezoelectric actuators are used in microelectromechanical systems (MEMS), microrobots, bioengineering and medicine, as well as in the fields of vibration and noise control.

The voltage generated in the mirror by the piezoelectric layer depends on its Jung module, piezoelectric module d_{mn} and applied electric field. Piezoactuators are divided into monomorphic and bimorphic. The first can be linear or shear type. Linear piezoactuators receive a signal applied parallel to the direction of polarization of the piezoelectric material and create force and deformation (d_{33}) in the same direction. The shear type piezoactuator detects a signal applied parallel to the polarization direction of the piezoceramic material and creates force and deformation (d_{31}) perpendicular to the applied voltage [27].

The design of the most common shift monomorphic DM (mode d_{31}) is presented in Figure 2. The active layer of piezoceramic *3* is firmly glued to the mirror substrate *1*. Between the substrate and the piezoceramic layer there is a grounded electrode *5*, and a set of electrodes *4* on the outer surface of the layer. Each electrode is controlled independently by the supply of electrical voltage. As a
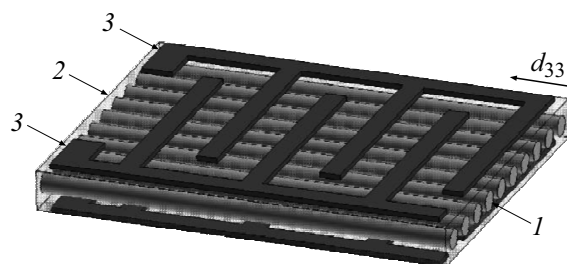
result, the transverse piezoelectric effect causes tension in piezoceramics, leading to the bending of the mirror.

There is also interest in linear piezoactuators [28–30]. It is explained by the fact that in many perovskite ferroelectric materials the constant d_{33} is about twice as much as d_{31}. But if piezoactuators in the d_{31}-modes have parallel plate electrodes, then piezoactuators with mode d_{33} are coated with interdigital electrodes. In addition, a device in d_{33} mode has a relatively complex structure as compared to d_{31}.

Lead titanate ceramic pervoskite zirconate $Pb(Zr_xTi_{1-x})O_3$ (LZT) is the most common piezoelectric product due to its large d-ratio and relatively low price. The most effective is the composition with $x \approx 0.52$.

In contrast to monomorphic DM, a bimorphic bending device consists of two piezoelectric thin plates with polarization perpendicular to the interface plane. A bimorph assembled from two plates whose polarization direction is identical is called a parallel bimorph. A bimorph in which the polarization of the plates has the opposite direction is denoted as a consecutive bimorph. During the supply of voltage due to the reverse piezoeffect, one of the layers expands, while the other is compressed or remains passive, causing the piezoactuator to bend [31–37].

Nonlinear hysteresis is one of the inherent characteristics of piezoelectric materials, which affects the operation of the piezoactuator. This characteristic has been well studied and can be compensated by operator or differential models [38]. Another important characteristic to consider is the creep [39]. It causes slow drift during the actuator operation. Hysteresis, as it seems, and the creep [40] can be loosened with the Prandtl−Ischlinski [41–43] reverse model. It has also been found that the [44] small residual curvature drift caused by piezoelectric creep can be easily minimized by applying small dynamic impulses of corrective voltage to bimorph electrodes.

The nature of ceramic monolithic piezoelectric materials makes them fragile and vulnerable to accidental breakage during manipulation and gluing, as well as during the scheduled maintenance. In addition, they fit poorly to curved surfaces. These limitations prompted researchers to develop alternative methods of piezoceramic production to make them more suitable for the next generation of piezo-

electric applications. To solve the problem of unsuitability of monolithic piezoceramic material for many applications, the idea of using a composite material consisting of an active piezoceramic fibrous phase, introduced into the polymer matrix phase, has been proposed. Typical composite configuration with active fibers is shown in Fig. 3 and includes a monolayer of one-axis oriented piezoelectric fibers embedded in a polymer matrix between two counter-pin surface electrodes through which the control voltage is supplied. The advantages of the active fiber composite configuration are that the electrical field is applied in the direction of the fibers operation and direction, which results in the use of the larger piezoelectric ratio d_{33}. The introduction of fine fibers typically less than $250\,\mu$m in diameter into a polymer matrix also means that the composite has a certain degree of flexibility and can fit the shape of irregular structures [45–47]. It has also been suggested that the combination of interdigital electrodes and ceramic fibers provides increased toughness and damage resistance, because the breakdown of individual fibers does not result in the final failure of a composite with active fibers.

2.4. Electromagnetic actuators

Magnetoactive materials are a new alternative to electro-active materials to create bimorphic deformation of the mirror [48–50]. Magnetostriction is a common phenomenon in which ferromagnetic materials expand or contract depending on the presence of a magnetic field.

Magnetic „smart“ material [51] s applied to the mirror substrate and covered with magnetic solid material. The magnetic recording head crosses the rear surface of the mirror and locally magnetizes the layers, transmitting deformation to the mirror. Due to the hard magnetic material, the localized change in DM shape is retained until it is actively demagnetized, as is the case with magnetic recording media. These drives are very reliable, practically do not exhibit hysteresis, aging or creep.

2.5. Temperature actuators

One possible use of adaptive optics in synchrotron and possibly laboratory X-ray systems is the monitoring and correction of deformations of the working surface of optical elements due to thermal load of the beam, gravity or environmental factors. Thermal distortions are particularly important, and an adaptive optical system that allows cooling with dynamic correction is highly desirable.

Optical substrates exposed to X-ray with high thermal load are usually deformed into convex shape („hump“). For reflective optics, this results in an increased bundle flow, for refractive optics — to the loss of X-ray bundle intensity. Therefore, these optical elements need to be cooled to emit heat, and correct their adverse thermal deformations [52].

By applying spatially-targeted heating and (or) cooling, it is possible to achieve sub-nanometer control of the DM
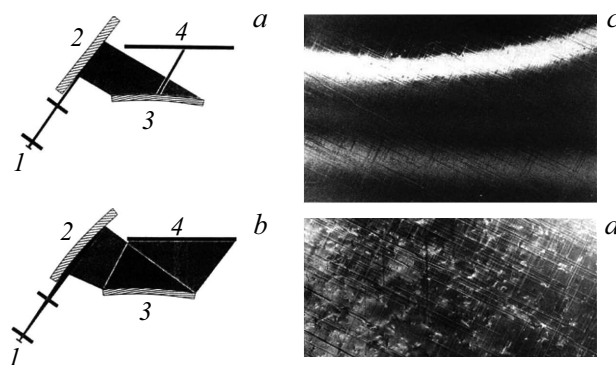
Figure 4. Diagram of the double-crystal diffractometer (a, b) and X-ray topograms of the bent GaAs crystal with heteroepitaxial film (c, d): *1* — X-ray source, *2* — asymmetric crystal monochromator, *3* — bent sample, *4* — photographic plate. *a*) The flat monochromator forms a flat wavefront, the diffraction condition is only fulfilled for the narrow area of the curved sample (c). (b). The curvature of the monochromator is adapted to the curvature of the sample, and the diffraction condition is fulfilled on most of the samples (the structure of misfit dislocations is clearly visible) (d) [57].

surface shape for X-ray radiation and high power [53]. For example, in the work [54] compensation of the uneven thermal load was carried out by introducing an external source of space-controlled electric heating, which reduced the temperature gradients causing distortion of the mirror shape. The electric heaters consisted of a series of cells arranged along the length of the mirror.

3. Adaptive optics for laboratory X-ray sources and SI sources

The characteristics of the X-ray beam can be greatly improved by compensating for the distortion of the wavefront caused by heat load, optical drift or the contribution of prior or subsequent optics. Different methods are used to correct the wavefront using refractive or reflective optics. The methods fall into two general categories. The first uses specially designed and manufactured corrective optics for static correction. The second category uses a deformable optical element that can be dynamically adapted to provide a variable correction.

Methods of static correction require the preliminary measurement of the wavefront or a priori knowledge of its form [55]. Apparently, the static correction of the wavefront was first used by the authors of the work [56] in the double-crystal X-ray topography for the study of homogeneous curved samples: during the experiment, the curvature of the monochromator crystal adapted to the curvature of the sample (Fig. 4). As shown in works [58,59], a static correction of the wavefront formed by the first crystal of a double-crystal X-ray monochromator exposed to the thermal load of a SR beam can be performed by a second monochromator crystal.
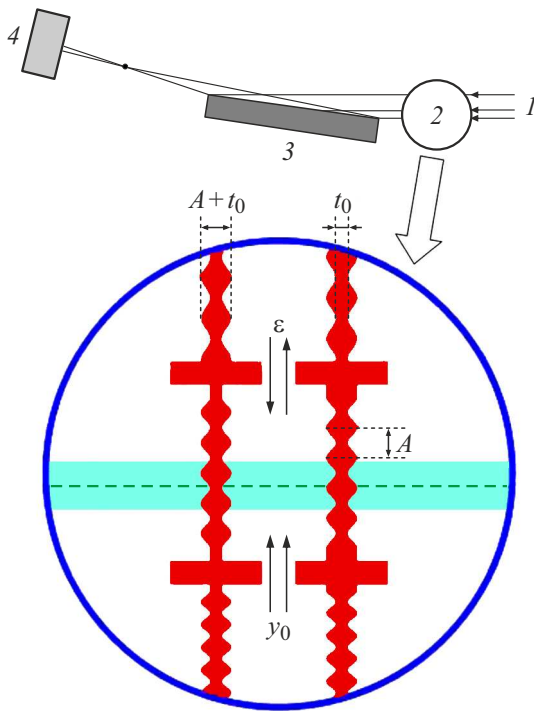
Figure 5. Experimental installation scheme with wavefront correction: *1* — X-ray beam with distorted wavefront, *2* — adaptive optics, *3* — focusing mirror, *4* — detector. On the insert a phase compensator is shown: vertical movements of y_0 and ε change the phase and amplitude correction of the wavefront respectively [55] (see text).

In work [60], compensation of X-ray optical system aberrations is carried out by the corresponding X-ray phase plate located behind the optical system. The phase plate operates on passage and is based on X-ray refraction. Therefore, it is largely insensitive to small surface inaccuracies of a few micrometres in shape. The phase plate can correct residual aberrations caused by surface errors of reflective optics, deformations in diffraction optics and accumulated surface errors in large refractive lens packets.

A deformable mirror can help compensate for shape errors caused by finite focusing optics that are not produced with sufficient accuracy. One adaptive element can adjust the sum of all these effects without having to fully understand the origin of each component. In the work [61,62], the refractive phase plate was used to compensate for the residual errors of manufacturing the optical system located beyond the plate.

However, this corrective optics only works with the optical element for which it was designed, and therefore has limited applicability. The work [55] describes a new form of adaptive corrective optics that allows dynamic correction of the wavefront. The adjustable corrector consists of a pair of refractors with a calculated thickness profile, so that the change in their position allows the precise adjustment of the wavefront. The length of the X-ray path in each structure is a sinusoidal profile with a period Λ, but with

phase two structure shifted by $\Lambda/2$ relative to the first, when differential translational offset between two structures $\varepsilon = 0$ (Fig. 5). The structures are located close to each other at a small distance before focusing optics and on the same line with the X-ray bundle, so the length of the X-ray path in the structures is

$$t(y) = 2A \sin(2\pi\varepsilon/\Lambda) \cos\big((2\pi/\Lambda)(y - y_0)\big) + 2(A + t_0),$$
$$(5)$$

where A — the structure amplitude, t_0 — the minimum structure thickness required to strengthen and ensure the stability of the manufactured structure, y_0 — the overall translational offset.

From the equation (5) it follows that the amplitude of the cosine member can be changed from $-2A$ to $+2A$ by changing the differential displacement ε between two structures from $-\Lambda/4$ to $+\Lambda/4$, and phase can vary from $-\pi$ up to $+\pi$ by moving both structures in the same direction in the range of $y_0 = -\Lambda/2$ up to $y_0 = +\Lambda/2$. This provides dynamic correction of the wavefront with a sinusoidal profile and variable amplitude and phase [55].

The authors of the work [63–66] proposed a dynamic adaptive optical system in which DM is placed before focusing optics to compensate for the wavefront errors it creates (Fig. 6). In this optical system, the angle of grazing incidence of the compensating mirror be smaller than that of the focusing mirror. The advantage of this design is that the required accuracy for the compensator mirror surface decreases faster than that of the focusing mirror, proportional to the angle of the sliding down compensator and focusing mirror (formula (1)). This means that a less accurate adaptive mirror can easily compensate for the distortion of the wavefront caused by the very small error in the shape of the focusing mirror. However, in this adaptive optical system, a *in situ*-phase error distribution assessment is needed to correct the bending of the compensating mirror.

4. Active optics for sources SI

Each SR channel after the ondulator section usually starts with a mirror used in a sliding fall and directing the radar bundle to the experimental station. It will adsorb part of the bundle, causing a heat stroke that will distort the shape of its surface and wavefront. The thermal impact will vary depending on the energy of the beam and the angle of slip, so it is not possible to adjust the situation for one operating mode. For this reason, the mirror must bend and deform in a controlled way to correct the deformations caused by the heat stroke. In X-ray optics, the grazing incidence configuration means that the bundle illuminates the mirror on a very long fringe one axis is longer than the other by two or even three orders of magnitude. For this reason, adjustments are usually made in this direction only.

The variable beam track („footprint"), much smaller than the mirror length, causes temperature change in tangential direction. The resulting thermal deformation of the surface shape, which is formed by the action of the beam, is not
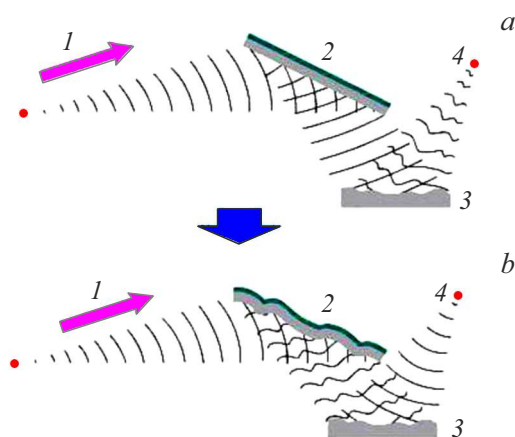
Figure 6. Concept of adaptive optical system for focusing X-ray radiation: *1* — X-ray spherical front propagation direction, *2* — adaptive mirror, *3* — focusing mirror, *4* — focus. In the top picture (*a*) the surface profile of the deformable mirror is flat, and the wavefront of the X-ray beam reflected by the focusing mirror is distorted due to errors in the shape — focusing is not ideal. In the lower Figure (*b*), on the contrary, the surface profile of the input mirror is deformed to compensate for the wavefront error. The result is a perfectly focused bundle X-ray [64].

cylindrical and therefore it is difficult to correct it with a mechanical bending machine [53]. The idea of the cooling system REAL [53] is to compensate for the uneven thermal load by introducing an external source of space-controlled heating, which will reduce temperature gradients causing mirror shape distortion. Since the photon beam can vary in intensity and flow, heaters must provide an adjustable heating length by adjustable heating capacity. Using a spatially variable heating profile, sub-nanometer surface shape control for medium- and high-power X-ray radiation was achieved.

In another design of the mirror holder [67], the mirror reflection error is minimized by water cooling of variable length. The simplified solution uses five cooling circuits along the beam track. The mirror cools on one side only. It has a chute located in 5 mm from the surface in which the eutectics GaIn is located.

However, most of the grazing incidence DM at experimental SR stations were implemented on the basis of the controlled bending of the substrate using piezoactuators [34,68–72]. In work [70], an active X-ray mirror is described with a substrate size of 35×40.8 cm and 10 drives along the entire length to create variable elliptic profiles. The mirror, created by the authors of the work [71], had a length of 40 cm, a width of 4 cm and was equipped with 13 piezoactuators. An X-ray DM with single crystal silicon substrate 45 cm, height 3 cm, and width 4 cm,is described in work [72]. Each of the 45 actuators has a length of 1 cm, a height of 3 cm, and a thickness of 0.15 cm. The actuators are evenly arranged every 1 cm along the tangential axis of the mirror. They are fixed with epoxy resin on the side

opposite to the reflective surface of the mirror. This allows the mirror to take both concave and convex shape.

The development of a set of optical components that simultaneously meet the requirements of high flow, high energy with wide fringe width, and efficient and variable focus, was a serious problem that could not be solved by the structures for a long time, used on most SR channels. In the work [73] the first application of a bimorph mirror with multilayer coating on the SR channel is described. To increase the aperture and pass- fringe, the elliptically curved silicon substrate surface was covered with three multi-layered fringes (Ni/B$_4$C, W/B$_4$C, Pt/B$_4$C) 1 m long. The thickness of d of each bar was chosen so that the Bragg angle of the first order of reflection was 4.2 mrad in the center of the mirror. Each fringe selects an X-ray with an energy of 40.0, 65.4 and 76.6 keV. In addition, each fringe was made with a lateral gradient along the length of the mirror to ensure high reflectivity of the entire strip. Sixteen piezoelectric bimorphic drives attached to the sides of the mirror substrate could adjust the shape of the reflective surface. This allowed the mirror to vary the focus distance from 3.6 to 4.8 m and compensate for residual shape errors. Focal spots with a vertical width of $< 15\,\mu$m were obtained in three positions in the range of 0.92 m with quick and easy switching from one focal position to another.

Deformable mirrors with mechanical bending do not have sufficient deformation accuracy. Piezocontrollable DM do not have long-term stability due to the drift of piezoelectric actuators, they also suffer from the coupling effect [74], which causes deformation errors in the gaps between the actuators.

The deformable mirrors used in the work [75,76], are hybrid systems consisting of a piezoelectric bimorph mirror and a mechanical bending device. In this configuration piezoelectric actuators on DM make a very small correction to the shape error after mechanical bending. The mechanical bending device approximates the required elliptical shape of the mirror surface, while the piezoelectric actuators attached to the mirror correct very small residual shape errors. The most significant advantage of this system is that the deformation of piezoelectric elements can be minimized. Thus, deformation drift, which is proportional to the deformation, can be significantly reduced. In addition, the system has the added advantage of being able to use long DM. Long piezoelectric bimorphic mirrors require piezoelectric plates of more than ~ 400 mm — as long as conventional piezoelectric bimorphic mirrors. However, they cannot be manufactured as long monolithic plates, and therefore multisegmented plates should be used instead. Since there is no bending moment in the clearance area between the segmented plates after gluing to the mirror substrate, significant deformation errors occur. This is called the transition effect [32]. In contrast, in the hybrid system this effect is significantly reduced because the bending moment is provided by a mechanical bending device. Since the restrictions on the manufacture of piezoelectric plates
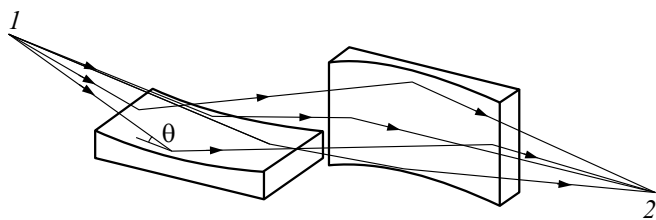
Figure 7. X-ray focus system scheme KB: *1* — X-ray point source, *2* — focus, θ — slip angle.

will be lifted, it will be possible to manufacture very long deformable mirrors (> 1 m in length) [76].

It is well known that astigmatism is completely eliminated by a system with crossed mirrors in which each mirror corrects the astigmatism of the other. Because the simple way to correct spherical aberration is to use aspherical mirrors, the most promising full external reflection (PWR) mirroring system for X-ray microfocusing should be considered a system of crossed aspheric mirrors (Kirkpatrick−Baez (KB) configuration [77]). The reflective surfaces of the mirrors may be in the form of a parabolic cylinder in the case of a collimating optic or elliptical cylinder in the case of focusing optics. The simplest focusing KB system is shown in Fig. 7. It consists of two cylindrical mirrors with the same radii of curvature and forms a real point image of a point object.

To focus the X-ray, a pair of multi-segment bimorphic mirrors in the KB configuration was used by the authors of the work [78]. KB mirrors create a minimum focal spot of $30 \times 24\,\mu$m. Bimorphic mirrors allow the bundle to refocus both horizontally and/or vertically within minutes to a bundle size of $150 \times 70\,\mu$m without significant loss of photon flow. The bundle size can be adapted to the sample size by adjusting the curvature of bimorphic KB mirrors. This operation can be performed within minutes with excellent reproducibility.

The authors of the work [75,76,79] constructed a two-stage adaptive mirror system KB using four piezoelectrically deformable DM. The use of four DM allowed the formation of a collided X-ray bundle with a variable shear section with a parallelism of $\sim 1\,\mu$rad or focus X-ray with variable focus size without the need to change the position of the mirror or sample by simply deforming the four mirrors.

5. Active optics for X-ray telescopes

Many astrophysical objects, such as a galaxy cluster, black holes in active galactic nuclei (AGN), galactic objects (supernova remnants, neutron stars), radiate, fluoresce or reflect X-ray [80]. The Earths atmosphere is an insurmountable obstacle to X-ray photons, so astrophysical research in this energy range is carried out directly from spacecraft. To obtain images, X-ray telescopes must use grazing-incidence mirrors that reflect the falling photons at very small angles. High-resolution X-ray mirrors typically

use a Wolter geometry of type I [81] in which the reflection from the parabolic to the hyperbolic surfaces creates a two-dimensional focus. Due to small grazing angles (usually $1°$ or less) the area of the collection is a small part of the mirror surface. To increase the effective area of the telescope, several coaxial and confocal mirrors with decreasing radii („mirror shells") are used, nested into each other like a Russian nesting doll, with the grazing angle decreasing from the outer shell to the inner one [82] (Fig. 8).

Space applications require X-ray mirrors to meet a number of requirements that could compromise the telescopes optical performance. In particular, they require compliance with the logistics of the scientific mission, which imposes limits on the telescopes mass: a large mass is indeed inevitable when it is required to have a large collection area, excellent angular resolution, and good thermomechanical stability of the optics. The practical production of Wolter I X-ray optics should take into account all these requirements, which are often contradictory. Low weight and large collection area are achieved by using several concentric very thin coating shells with a high atomic number, such as iridium, for good reflection efficiency. However, the reduction in the thickness of the mirror shells makes the
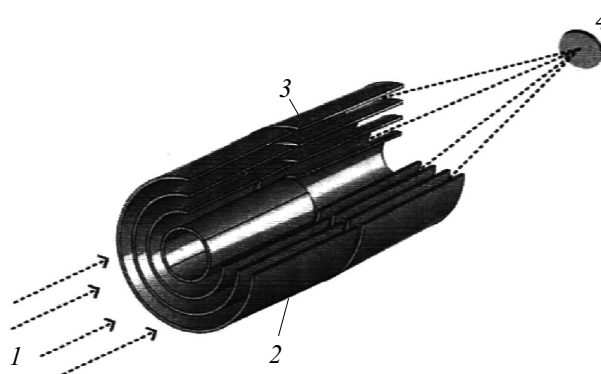

Figure 8. The radar stroke in the multilayer Wolter mirror I. When focusing X-rays (*1*), reflecting successively from the parabolic (*2*) and hyperbolic (*3*) surfaces of each mirror shell, are assembled in the focal plane (*4*) [81].
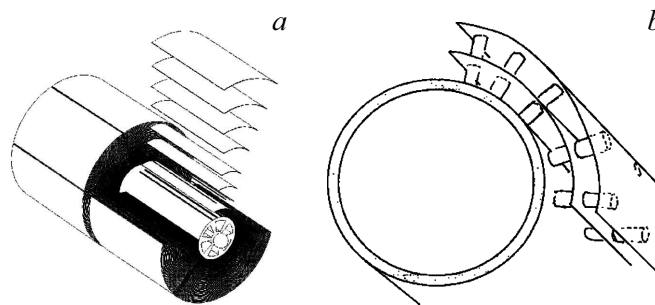

Figure 9. (*a*) Geometry of mounting of telescope optics consisting of 72 casings [89]. (*b*) Discrete (piston) surface-normal drives for adjustment and correction of the shape of grazing-incidence mirrors, acting radially on the successively nested shells [87,88].
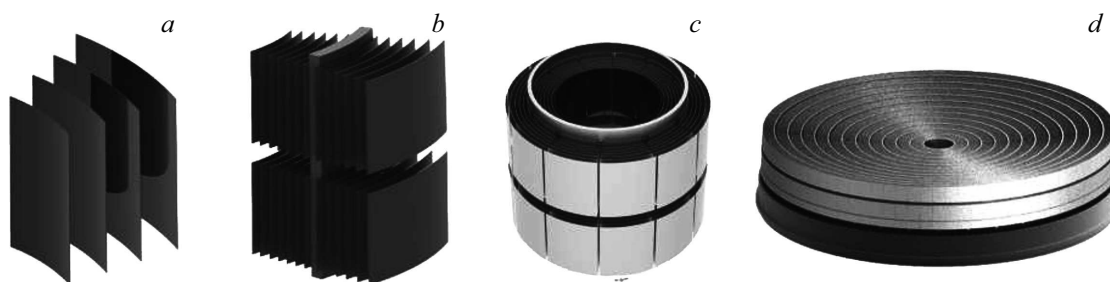
Figure 10. The stages of X-ray mirror production are based on the example of mirror assembly for the observatory *Lynx*: 37 492 mirror segments (*a*) are integrated into 611 mirror modules (*b*), which in turn are combined into 12 meta-shells (*c*); 12 meta-shells are integrated into a full assembly (*d*) [96].

optics less rigid. Such stiffness decreasing makes the mirror more susceptible to random loads and distortion, which can degrade its shape.

X-ray telescopes with a high effective collection area usually use the integration of a large number of thin mirror segments in a very compact arrangement [83] (Fig. 9, *a*).

Segmented mirrors offer several advantages over full mirror shells. Due to its modularity, segmented design facilitates mass production. This approach has the advantage that large mirror assemblies do not require a proportionately large infrastructure. Perhaps more importantly, due to the relatively small size of the mirror segments, the segmented approach allows for very light mirrors and the use of commercially available equipment, materials and modern mass production technologies.

To create a lightweight segmented X-ray telescope with large effective area and good angular resolution, the thin glass foils [84] produced by high-temperature sediment of thin sheets of glass [85,86] are successfully used. In essence, there are two categories of actuators that differ in the way they apply force to the mirror. For adjustment or for general or local deformations of the mirror, surface-normal drives acting as a piston can be used (Fig. 9, *b*). They are suitable for the adjustment and correction of some form errors. Surface-tangent actuators in combination with mirror substrate act as bimorph for local mirror deformation [87].

Radially adjustable grazing incidence mirrors are a potentially inexpensive approach that significantly improves the resolution of existing thin mirrors to a few arc seconds for a moderately efficient visual field. These mirrored assemblies consist of a precision manufactured lightweight cylindrical or conical core, on the outside of which a series of axial rows of electro-shock actuators is attached. Bi-directional adjustment for the segment set adjacent to the core is performed first by displacing all the regulators to their approximate mean points, so that the increased or decreased voltage causes a radial displacement outside or radially inward, respectively. After adjusting/regulating the first shell or set of segments, the next set of controls is glued to the back sides of the mirror segments, then the next „layer" of mirror segments is applied. The process is repeated until all mirrors are successfully mounted and
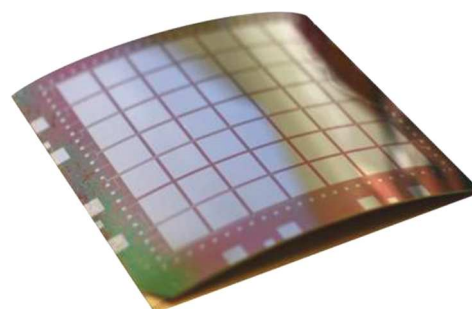

Figure 11. Array of 7×7 piezo elements measuring 10×10 mm applied to a cylindrical glass shell measuring 100×100 mm and radius of curvature 220 mm. In the picture the side reflecting X-ray is facing down [98].

adjusted, and their lower values are corrected. This process should lead to a relatively stable structure that would correct shape errors such as axial slopes and deflections [88].

Active optics should be selected so that it not only improves the mirror shape, but can also be incorporated into the mirror module without adding a substantial thickness or structure to the gap between adjacent nested mirror shells that would cover the X-ray path. Therefore, it seems preferable to use surface-tangent actuators with the possibility of more flexible correction of the shape of mirror shells [89–95].

Large mirrored assemblies designed for future missions are typically divided into many wedge-shaped modules, both radially and azimuthally. This approach has the advantage of requiring many identical modules of a small size. The modular X-ray mirror assembly steps are shown in Fig. 10. The ability to dynamically adjust the shape of the DM allows you to control the mirror shape after installation or even after launch (i.e., make corrections in orbit) [96].

In response to demands for high effective area and high angular resolution, the Smithsonian Astrophysical Observatory (SAO) developed the concept of using pixel active components in segmented sliding-drop optics. The variant of the SAO concept of a bimorphic array of a separate segment is shown in Fig. 11. The optics contain 8400 segments with a thickness of $\sim 0.2-0.4$ mm, creating 292

nested shells. Each segment has a thin film of piezoelectric material applied to the back of a very thin mirror with an active 40×40 mesh of individually addressed actuators. As a result, with 1600 executive mechanisms in each segment and 8400 segments, we have $\sim 10^7$ of active components, which greatly complicate the telescope design [97].

To simplify the construction, a line/column addressing scheme using ZnO (TFT) thin-film transistors applied on top of the insulating layer on the back of the piezoelements is proposed in the work [99]. The concept is aimed at the realization of electrical connections through anisotropic conductive film, which is used in liquid crystal displays. It is also proposed to connect the strain gauges to cells that can be used to determine changes in the voltage/piezomaterial ratio, which will facilitate any necessary adjustment in orbit.

Wires hanging on the back of the foil will prevent the penetration of X-ray in tightly packed casings, and because of their weight the thin sheath will deform. Therefore, the authors of the work [95] proposed to apply the contacts directly to the back of the mirror using photolithography (Fig. 12).

6. X-ray adaptive and active opticsmetrology

To optimize adaptive and active optics systems, accurate information on the wavefront of a focused X-ray beam is required. Therefore, before adjusting the wavefront phase, it must be measured. Recently, metrology of X-ray optics *in situ* is usually carried out using the methods of „at-wavelength metrology" [101,102]. The wavefront sensor is one of the elements of the metrology system. Its task is to measure the curvature of the wavefront and transfer these measurements to the processing device. There is a wide variety of wavefront sensors [103]. Among them are the Shack−Hartmann sensors, as well as sensors based on the Talbot effect, X-ray specks and ptychography.

6.1. Shack−Hartmann wavefront sensors

One of the most common methods for measuring the wavefront are the Hartmann and Shack−Hartmann sensors. They can operate in real time, independent of wavelength, and work with both coherent and non-coherent sources. These sensors are achromatic and can be compatible with different types of X-ray sources.

The Hartmann wavefront sensor consists of a matrix X-ray detector (usually CCD or CMOS) and a mask with symmetrical hole pattern. Each hole corresponds to a spot on the detector. In case of registration of a flat wavefront, all distances between the spots will be equal, and if the incoming bundle suffers from aberrations of the wavefront, in the plane of the image will deform the grid of spots. The offset of the spot on the detector corresponding to a certain hole in the mask is proportional to the gradient of the wavefront [104]. After the recovery of the wavefront

Figure 12. System of metal electrodes applied to the reverse side of the glass shell. You can notice the azimuthal curvature, previously created by the process of high temperature shell forming [93].
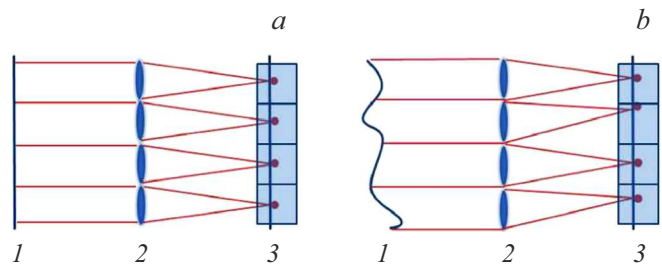

Figure 13. Shack−Hartmann wavefront sensors The input flat wave (*a*) is focused by a grating of lenses, resulting in a grid of focal spots on the detector. If the wavefront is distorted (*b*), the focal spots are displaced relative to the original grid. *1* — wavefront, *2* — grating of lenses, *3* — grid of focal spots on the detector [108].

gradient map using the wavefront reconstruction algorithm, the wavefront itself is restored [105–108]. The main advantage of the method is that it uses a very simple optical system, its main drawback is the need to calibrate the detector [109,110].

The Shack−Hartmann method is a variation of the classical Hartman method with the difference that instead of a diaphragm mask, a microlens array is used to break the wavefront into multiple parts, each forming a separate focal spot [111] (Fig. 13). There are several possible implementations of the Shack−Hartmann X-ray sensor. It can be a set of zone plates [112] or refractive lenses [113,114].

6.2. Talbot interferometer based wavefront sensors

In 1836 Talbot [115] discovered that if the primary coherent wave diffracts on a periodic structure, such as a diffraction grating, behind this structure there is a self-replication of its image at distances

$$L_T = 2md^2/\lambda,$$

d — grating period, $m = 1, 2, 3, \ldots$. This phenomenon is called „Talbot effect", and distance L_T — „Talbot distance". Subsequently, the [116] fractional Talbot effect was also discovered, i.e., the self-image of the phase grating could be observed [117] at distance

$$L_m = md^2/2\eta^2\lambda. \qquad (6)$$

Interference from the phase grating will always have maximum contrast at odd orders ($m = 1, 3, 5, \ldots$), at that time as the amplitude grating will give maximum contrast at even orders ($m = 0, 2, 4, \ldots$). $\eta = 1$ ratio if the grating is an amplitude or phase grating with a phase shift of $\pi/2$, and $\eta = 2$ if the grating provides a phase shift for π.

The fractional Talbot distance in the case of a spherical wave shall be

$$L_m = R_0 m d^2/(2\eta^2 R_0 \lambda - m d^2), \qquad (7)$$

where R_0 — distance from the source of radiation to the grating.

The grating pitch must be adapted to obtain the allowable pattern in the detector plane: too small a step will lead to an unresolved moire pattern, at then time as a large step will reduce the angular sensitivity of the device. At wavelengths of hard X-ray radiation, the period d_1 phase grating should not exceed a few microns. In this case the interference fringes will have an interval in the micron range, which is beyond the resolution of most detectors, especially those with a sufficiently large field of vision. You can solve this problem by placing in the detection plane at a distance L_m an absorption grating with pitch

$$d_2 = d_1(R_0 + L_m)/2R_0.$$

Thus, a grid interferometer consists of a phase grating acting as a light divider and an absorption grating acting as a pass mask [118] (Fig. 14).

As a rule, a grid interferometer is used in the moire fringes analysis mode, where two grating are tilted relative to each other at a small angle [119,120]. The analysis of the distortion of the moire fringes makes it possible to characterize the aberrations of the wavefront of the wavelength order. The radius of curvature of the wavefront of X-ray radiation and its distortion can be accurately measured from one image [121].

The radius of curvature of the wavefront R is related to the slope angle of the moire fringe ϑ_m [120,122]:

$$R^{-1} = R_0^{-1} - d_2 \tan \vartheta_m/d_m L_m, \qquad (8)$$
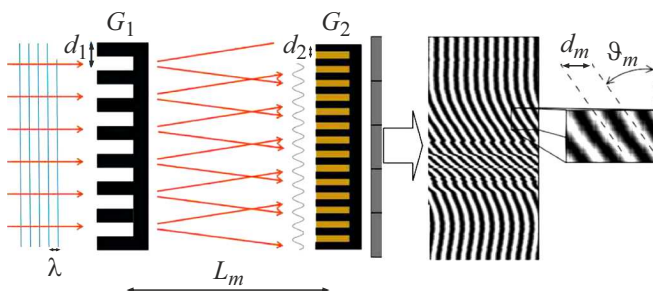
where d_m — fringe spacing (Fig. 14).

Figure 14. Talbots interferometer scheme (G_1 and G_2 — phase and amplitude grating with a period of d_1 and d_2 accordingly) and the resulting moire painting (d_m — distance between the fringes, ϑ_m — moire fringe inclination) [118,119].

Advanced and specialized analysis of X-ray interferometry [123,124] data is required to process information and obtain real physical results. Phase information can be recovered either by the Fourier analysis based on the moire effect [125] or by the step-by-step phase change method in the lattice interferometry [126]. The use of the Talbot interferometer to compute wavefront tilt error has already been reported [102,103,118,121,122,127]. The use of a two-dimensional lattice interferometer [128,129] for this purpose was also reported, which allows both horizontal and vertical gradients of the X-ray bundle phase from a single two-dimensional raster scanning. Other lattice methods are used, some of which use a single grating [130–134]. For example, in the work [131] an interferometer without a second grating is described, because the fringe pattern enlarged by the optical system can be recorded directly without the moire effect. Single grating methods are particularly useful for assessing the wavefront of highly divergent bundles [130].

6.3. Wavefront sensors based on X-ray speckles

The wavefront and associated aberrations can be accurately measured using a speckle-based method. When a scattering diffuser consisting of small objects is placed in a fully or partially coherent X-ray bundle, the speckle structure of the passing field [135] can be recorded using a high spatial resolution detector.

One interesting property of short-field speckles ($L \ll a^2/\lambda$, where a — the size of the pattern element, L — the distance between the sample and the detector) is that the radiation propagation distortion is determined solely by the wavefront form.

The key idea of the method is that each subset of images contains a distinct pattern of spots of different size and shape, which acts as a single marker, and can be tracked numerically between images taken at different times or in different planes. In other words, speckle-based methods use high-frequency random wavefront intensity modulations whose fine details act as markers to determine the X-ray trajectory [136].

The newly developed metrology method, based on X-ray speckles, has proved promising due to the ease of experimental installation, high angular resolution and moderate requirements for mechanical stability [137–144].

The advantage of the speckle method lies in its low coherence requirements and the quality of the wavefront modulator, such as a piece of sandpaper or biological filter. The method can be implemented in two modes: „absolute" and „differential" [141]. In the absolute configuration the membrane or sandpaper are placed before the examined optics (Fig. 15, a), and the first derivative of the wavefront is calculated. In the differential configuration the membrane or sandpaper is placed behind the focal plane (Fig. 15, b), and the second derivative of the wavefront is measured, namely the value of its local radius of curvature. This mode takes into account the imperfections not only of the optical
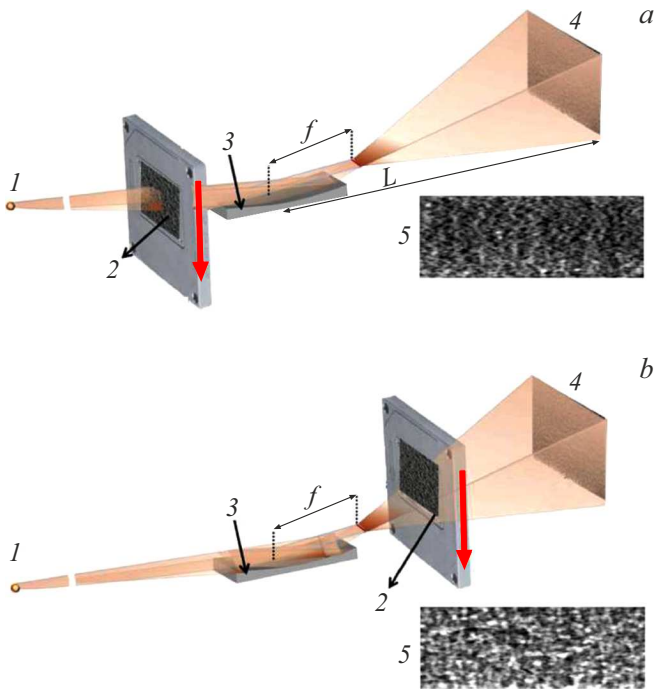
Figure 15. Experimental installation scheme for wavefront characterization in absolute (*a*) and differential (*b*) modes:*1* — radiation source, *2* — membrane (sandpaper), *3* — bimorphic mirror (*f* — its focus distance), *4* — detector, *5* — speckle-picture [142].

element being tested, but also of any optics before the measuring point [145].

In the absolute method, correlation analysis is used to compare speckled pictures obtained with and without the object. In the differential method, a higher spatial resolution can be obtained by scanning the phase modulator across the bundle, as the correlation uses subsets containing more pixels [144].

Speckle displacement is determined by the algorithm of mutual correlation of the two signals [146]. If the offset is calculated, it can be used to derive a vertical gradient of the wavefront $\alpha_y(x, y)$ [147]. Since the first wavefront derivative is directly proportional to the local phase shift gradient of the sample $\Phi(x, y)$, it can be written as

$$\partial \Phi(x, y)/\partial y = (2\pi/\lambda)\alpha_y(x, y) \approx 2\pi(L_1 + L_2 + L_3)$$
$$\times \upsilon(x, y)\mu/\lambda L_1 L_3, \qquad (9)$$

where $\upsilon(x, y)$ — speckle displacement, μ — scanning pitch, and L_1, L_2 and L_3 — distance between X-ray source, sample, sandpaper and detector respectively. It should be noted here that several (usually 3−5) adjacent pixels of the reference speckle image are selected to perform mutual correlation, so speckle displacement can still be tracked even with strong speckle bias perpendicular to the direction being investigated. Following the same procedure, a horizontal scan is performed to obtain a horizontal phase gradient. The
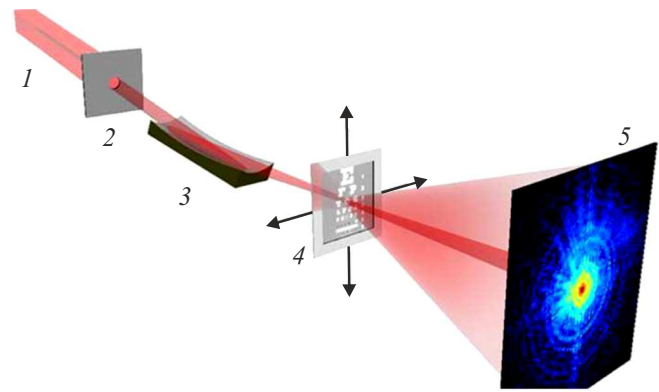

Figure 16. The geometry of the experiment to characterize the focused X-ray bundle. The diaphragm *2* selects a coherent portion of the SI *1* bundle that is focused by the examined mirror *3* on the test object *4*. The sample is scanned in a plane perpendicular to the direction of the bundle propagation. The diffracted radiation on the sample is recorded by the detector *5* [156].

phase shift induced by the sample is then recovered from two phase gradients [148].

When the wavefront is slightly inclined φ the local radius of curvature R of the wavefront is defined by the expression

$$R^{-1} = (\lambda/2\pi)(d^2\Phi/dy^2) = d\varphi/dy. \qquad (10)$$

Here Φ — phase wavefront, λ — wave length, y shows vertical direction. In the case of the differential mode the radius of the wavefront R_i for pixel i can be calculated [101,149,150] using the ratio

$$R_i/(R_i - L) = \sigma(i - j)/s_i, \qquad (11)$$

where L — the diffuser-detector distance, σ — the detector pixel size,i and j — the indices of the two selected rows on the detector, and s_i — the relevant distance in the diffuser plane between the bundle falling on pixels in i and j lines. Assuming that the diffuser is scanned in a linear pitch τ, you can build two speckle structures out of i and j lines in a stack of scan images. Using mutual correlation, it is possible to calculate a linear offset of ξ between two drawings, and then the distance between two rays in the diffuser plane is equivalent to the diffuser offset: $s_i = \xi_i \tau$ [150].

The two wavefront gradients, $\partial \Phi/\partial x$ and $\partial \Phi/\partial y$, are restored by a two-dimensional numerical integration method [151,152]. Finally, 2D-integration $\partial \Phi/\partial x$ and $\partial \Phi/\partial y$ gives the wavefront Φ [153].

6.4. Wavefront sensors based on ptychography

X-ray scanning coherent diffraction microscopy, also known as ptychography [154], is one of the most important methods for characterizing X-ray bundle and optics [155]. It can be used to quantitatively determine the complex wave field of focused X-ray radiation and therefore to detect errors of the wavefront with unprecedented sensitivity and
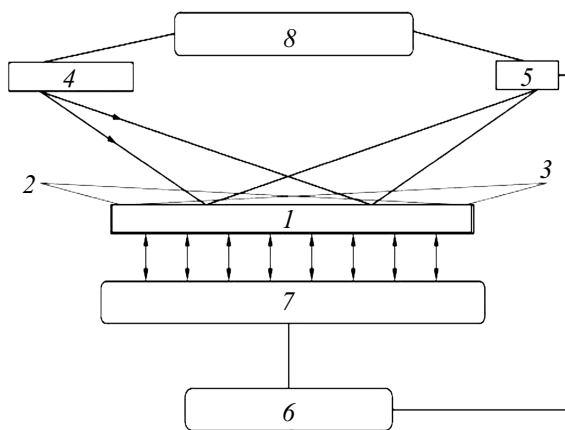
Figure 17. Cooling adaptive mirror system diagram for synchrotron X-ray radiation *1* — deformable mirror, *2* — X-ray source,*3* — focus, *4* — visible light source, *5* — Shack–Hartmann wavefront sensor, *6* — feedback controller, *7* — executing mechanism, *8* — visible light node controller [164].

spatial resolution [156,157]. In ptychography, the test object is scanned across a coherent X-ray beam, providing partial overlap of illuminated areas corresponding to adjacent exposures (Fig. 16). In each scanning position in the distant field $(L \gg a^2/\lambda)$ a diffraction pattern of the object is recorded. From the recorded diffractograms, the complex transmittance function of the sample and the complex wave field of the incoming X-ray beam can be restored using iterative numerical methods [158–160].

The key to correct reconstructions is a large number of diffractograms (in work [155], (15 876 diffractograms were collected, each encoding information about the wave field. Due to redundant information, wavefront recovery is very resistant to inevitable inaccuracies in scanning positions. Besides, the test object doesn't have to be exactly focus.

The method has the advantages: conceptually simple and not relying on slow converging iterative reconstruction algorithms, the method works in the case of high-energy X-rays $(> 6\,\text{keV})$ [161].

6.5. Wavefront sensors with feedback

The wavefront sensors discussed above generally provide feedback only periodically and usually invasively [162], interrupting the experiment and wasting valuable time. There are *in situ* feedback methods based on redirecting part of the X-ray flow to the wavefront sensors, thus making these photons inaccessible to the experiment [163]. For these reasons *in situ* real-time metrology methods for characterizing the wavefront without interrupting the experiment are preferred.

Non-invasive feedback can be done in various ways. For example, in the work [164] a source of visible light was included in the feedback system. The system consisted of a silicon mirror with a length of 1 m platinum-coated water-cooled, supported by two rows of piezoelectric drives

containing 11 elements each (Fig. 17). The shape of the mirror was constantly monitored by an optical analyzer, and its measurements were used by the real-time feedback loop to control the executing mechanism actuators, which adjusted the mirror shape.

The feedback method proposed in the work [165,166] is based on the use of a stable independent metrological frame with absolute position sensors mounted on it, which measure the deviation of the reflective surface of the mirror from the desired shape (Fig. 18). The metrological frame is fixed relative to the surface of the mirror approximately at the working distance of the sensors. In most rigid X-ray spectroscopic systems this distance is sufficient to allow an X-ray beam to touch the surface of the mirror directly below the front of the metrological frame, allowing the use of such a system for *in situ* monitoring during the experiment. Signals from the absolute position sensor array are used to generate feedback, providing real-time control of the mirror surface shape. Fiber position sensors function in the Fizo interferometer configuration [167].
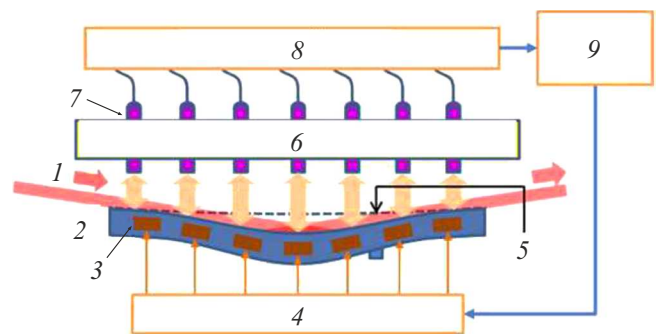

Figure 18. Closed-loop system architecture for active control of bimorphic mirror shape: *1* — X-ray beam, *2* — bimorphic mirror, *3* — piezoactuator, *4* — mirror, *5* — preferable shape, *6* — metrological frame, *7* — array of absolute position sensors,*8* — signal processing system, *9* — feedback controller [165].
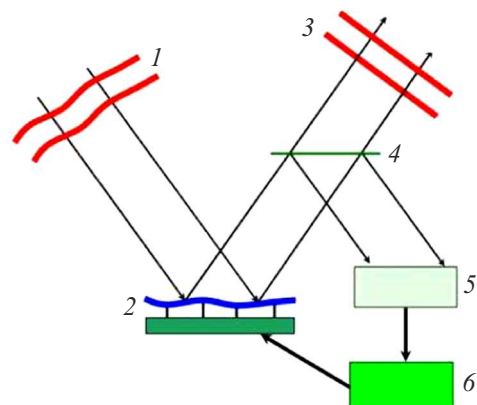

Figure 19. Non-invasive wavefront correction scheme using a light splitter:*1* — distorted wavefront, *2* — DM, *3* — „corrected" wavefront, *4* — beam splitter, *5* — wavefront detector, *6* — computer providing feedback [168].

Fig. 19 shows a circuit of active optics using a non-invasive sensor of the wavefront of visible light together with a light splitter [168]. The authors of the work [169–171] showed that a thin single crystal diamond plate can be used as a light splitter for X-rays.

7. Summary, findings and prospects

Active and adaptive X-ray optics has been used successfully for several decades in many scientific disciplines, including astronomy, laser physics, medicine, materials science, micro- and nanoelectronics, and the study of biological objects. Unlike passive optics with fixed, pre-polished surface profiles, active and adaptive optics can be deformed to fit different experimental problems.

The use of active wavefront control means with the help of adaptive optical elements, such as DM, provides precise control of the wavefront shape. One DM can adjust the sum of all these effects without having to fully understand the origin of each component.

This precise and „programmable“ control, not available for non-adaptive elements, leads to significant improvements in many optical systems. This is why adaptive and active optics are used in a wide range of applications to improve image quality and reduce aberrations.

In the future, concerted efforts are needed to create and develop cost-effective and reliable adaptive and active wavefront correction methods to actually improve existing X-ray optics. It is also necessary to develop and implement lead-free piezoelectric materials. Despite the good piezoelectric ability of lead-containing piezoelectric materials such as $Pb_xZr_{1-x}TiO_3$, due to the toxic effects of lead on the environment in the future, they should be gradually replaced by piezoelectric materials, not containing lead [172].

To use the brightness of modern X-ray sources effectively, the beam size must match the sample size. Alternatively, X-ray beams of variable size probing subdomains of larger samples can be used. In both cases the variation from sample to sample means that a different beam size X-ray may be required for each data collection cycle. Rapid changes in the size of the X-ray beam are usually made by changing the width of the apertures that determine the size of the beam. However, this is detrimental to the photon flow. The size change of the X-ray beam can also be achieved by changing the profile of the achromatic reflecting optics surface. Active optics have already been used to quickly and smoothly change the size of the X-ray focal spot from one micron to tens of nanometers [79]. This approach has the advantage of retaining the full radiation stream directed to the sample.

Development of high-speed active optics for X-ray radiation can fundamentally change the way of dynamic use of focusing elements on synchrotron radiation sources and free electron laser (FEL) and contribute to new scientific discoveries in the future.

Further development of high-speed active optics should help to improve *in situ* metrology, including feedback metrology.

For X-ray astronomy, in addition to further improving the technology of individual mirrors, it is important to formulate a strategy for diagnosing and correcting errors of adjustment and shape for a large number of mirrors, required for X-ray large aperture telescope consisting of a number of mirrored modules, each of which contains hundreds of highly nested segmented mirrors. To implement this strategy to determine and improve X-ray optics on the ground and in space will require the development of sophisticated control algorithms and auxiliary equipment. Since the diagnostic and configuration scheme can be complex and time-consuming, it is important that adjustment in space is infrequent. This, in turn, will require improved optical assembly on the ground, as well as excellent repeatability and stability of the executive mechanisms themselves.

There is no doubt that adaptive and active X-ray optics, with its flexibility and accessibility, will achieve even greater use in various fields of science and technology, overcoming all the difficulties in improving efficiency.

Conflict of interest

The author declares that he has no conflict of interest.

References

[1] H.W. Babcock. Pub. Astr. Soc. Pac., **65** (386), 229 (1953). DOI: 10.1086/126606

[2] V.P. Linnik. Opt. i Spektr., **25** (4), 401 (1957) (in Russian).

[3] N. Woolf. In: IAU Colloq. 79: *Very Large Telescopes, their Instrumentation and Programs* (1984), p. 221.

[4] R.N. Wilson, F. Franza, L. Noethe. J. Mod. Opt., **34** (4), 485 (1987). DOI: 10.1080/09500348714550501

[5] E.L. Church, P.Z. Takacs. Opt. Eng., **34** (2), 353 (1995). DOI: 10.1117/12.196057

[6] G.E. Ice, J.D. Budai, J.W.L. Pang. Science., **334** (6060), 1234 (2011). DOI: 10.1126/science.1202366

[7] M. Idir, L. Huang, N. Bouet, K. Kaznatcheev, M. Vescovi, K. Lauer, R. Conley, K. Rennie, J. Kahn, R. Nethery, L. Zhou. Rev. Sci. Instrum., **86** (10), 105120 (2015). DOI: 10.1063/1.4934806

[8] Y. Takei, T. Kume, H. Motoyama, K. Hiraguri, H. Hashizume, H. Mimura. Proc. SPIE, **8848**, 88480C (2013). DOI: 10.1117/12.2023940

[9] D.J. Bell, T.J. Lu, N.A. Fleck, S.M. Spearing. J. Micromech. Microeng., **15** (7), S153 (2005). DOI: 10.1088/0960-1317/15/7/022

[10] M.R. Howells, D. Camble, R.M. Duarte, S Irick., A.A. MacDowell, H.A. Padmore, T.R. Renner, S. Rah, R. Sandler. Opt. Eng., **39** (10), 2748 (2000).

DOI: 10.1117/1.1289879

[11] R. Barrett, R. Baker, P. Cloetens, Y. Dabin, C. Morawe, H. Suhonen, R. Tucoulou, A. Vivo, L. Zhang. Proc. SPIE., **8139**, 813904 (2011). DOI: 10.1117/12.894735

[12] O. Hignette, G. Rostaing, P. Cloetens, A. Rormneveaux, W. Ludwig, A. Freund. Proc. SPIE., **4499**, 105 (2001). DOI: 10.1117/12.450227

[13] L. Zhang, R. Baker, R. Barrett, P. Cloetens, Y. Dabin. AIP Conf. Proc., **1234**, 801 (2010). DOI: 10.1063/1.3463335

[14] P. Eng, M. Newville, M.L. Rivers, S.R. Sutton. Proc. SPIE., **3449**, 145 (1998). DOI: 10.1117/12.330342

[15] S.J. Chen, C.K. Kuan, S.Y. Perng, D.J. Wang, H.C. Ho, T.C. Tseng, Y.C. Lo, C.T. Chen. Opt. Eng., **43** (12), 3077 (2004). DOI: 10.1117/1.1813438

[16] J. Nicolas, C. Colldelram, C. Ruget, L. Ribó, P. Pedreira, P. de la Rubia, C. Martín-Nuño, D. Úbeda, A. Tomás. Proc. SPIE, **9965**, 996503 (2016). DOI: 10.1117/12.2239533

[17] I.T. Nistea, S.G. Alcock, P. Kristiansen, A. Young. J. Synchrotron Rad., **24** (3), 615 (2017). DOI: 10.1107/S1600577517005422

[18] D. Shu, A. Li, S.P. Kearney, C. Mao, J. Anton, R. Harder, X. Shi, T. Mooney, L. Assoufid. AIP Conf. Proc., **2054**, 060015 (2019). DOI: 10.1063/1.5084646

[19] W. Liu, G.E. Ice, J.Z. Tischler, A. Khounsary, C. Liu, L. Assoufid, A.T. Macrander. Rev. Sci. Instrum., **76** (11), 113701 (2005). DOI: 10.1063/1.2125730

[20] H. Mimura, H. Yumoto, S. Matsuyama, Y. Sano, K. Yamamura, Y. Mori, M. Yabashi. Appl. Phys. Lett., **90** (5), 051903 (2007). DOI: 10.1063/1.2436469

[21] B. Park. *Development of a Low Voltage and Large Stroke MEMS-based Lorentz Force Continuous Deformable Polymer Mirror System*. Thesis (University of Manitoba, Winnipeg, MB, 2018).

[22] X. Lv, W. Wei, X. Mao, Y. Chen, J. Yang, F. Yang. Sensors and Actuators A: Physical, **221**, 22 (2015). DOI: 10.1016/j.sna.2014.10.028

[23] S.A. Cornelissen, A.L. Hartzell, J.B. Stewart, T.G. Bifano, P.A. Bierden. Proc. SPIE, **7736**, 77362D (2010). DOI: 10.1117/12.857296

[24] S. Cornelissen, P. Bierden, T. Bifano, V. Charlie, J. Lam. Micro/Nanolith. MEMS MOEMS, **8** (3), 031308, (2009). DOI: 10.1117/1.3158067

[25] W.-M. Zhang, H. Yan, Z.-K. Peng, G. Meng. Sensors and Actuators A: Physical., **214**, 187 (2014). DOI: 10.1016/j.sna.2014.04.025

[26] H. Liu, J. Zhong, C. Lee, S.-W. Lee, L. Lin. Appl. Phys. Rev., **5** (4), 041306 (2018). DOI: 10.1063/1.5074184

[27] C.T. DeRoo, R. Allured, V. Cotroneo, E. Hertz, V. Marquez, P.B. Reid, E.D. Schwartz, A.A. Vikhlinin, S. Trolier-McKinstry, J. Walker, T.N. Jackson, T. Liu, M. Tendulkar. Proc. SPIE, **10399**, 103991M (2017). DOI: 10.1117/1.JATIS.4.1.019004

[28] V.D. Kugel, Sanjay Chandran, L.E. Cross. Appl. Phys. Lett., **69** (14), 2021 (1996). DOI: 10.1063/1.116866

[29] E. Hong, S.V. Krishnaswamy, C.B. Freidhoff, S. Trolier-McKinstry. Mat. Res. Soc. Symp. Proc., **687**, 316 (2002). DOI: 10.1557/PROC-687-B5.16

[30] Q.Q. Zhang, S.J. Gross, S. Tadigadapa, T.N. Jackson, F.T. Djuth, S. Trolier-McKinstry. Sens. Actuators A., **105** (1), 91 (2003). DOI: 10.1016/S0924-4247(03)00068-2

[31] J. Susini, D. Labergerie, L. Zhang. Rev. Sci. Instrum., **66** (2), 2229 (1995). DOI: 10.1063/1.1145715

[32] R. Signorato, O. Hignette, J. Goulon. J. Synchrotron Radiat., **5** (3), 797 (1998). DOI: 10.1107/S0909049597012843

[33] Q.-M. Wang, X.-H. Du, B. Xu, L.E. Cross. J. Appl. Phys., **85** (3), 1702 (1999). DOI: 10.1063/1.369314

[34] S.G. Alcock, I. Nistea, J.P. Sutter, K. Sawhney, J.-J. Ferme, C. Thellier, L. Peverini. J. Synchrotron Rad., **22** (1), 10 (2015). DOI: 10.1107/S1600577514020025

[35] J.P. Sutter, S.G. Alcock, Y. Kashyap, I. Nistea, H. Wang, K. Sawhney. J. Synchrotron Rad., **23** (6), 1333 (2016). DOI: 10.1107/S1600577516013308

[36] Y. Zang, M. Li, S. Tang, J. Gao, W. Zhang, P. Zhu. Nucl. Instrum. Methods Phys. Res. A., **860** (1) 13 (2017). DOI: 10.1016/j.nima.2017.03.053

[37] V.V. Gribko, A.S. Markelov, V.N. Trushin, E.V. Chuprunov. Instruments and Experimental Techniques, **62**, 703 (2019). DOI: 10.1134/S0020441219040183.

[38] H.A.S. Mohd, Z.A.M. Ahmad. Evolutions Mech. Eng., **2** (3), 000538 (2019). DOI: 10.31031/EME.2019.02.000538

[39] H. Jung, D.-G. Gweon. Rev. Sci. Instrum., **71** (4), 1896 (2000). DOI: 10.1063/1.1150559

[40] S.E. Alexandrov, E.A. Lyamina, N.M. Tuan. J. Appl. Mech. Tech. Phy., **55** (4) 682 (2014). DOI: 10.1134/S0021894414040142.

[41] L. Prandtl. Zangew. Math. Mech., **3**, 401 (1923).

[42] A.Y. Ischlinsky, D.D. Ivlev. *Mathematicheskaya Teoriya Plastichnosti* (Physizmatlith, M., 2001).

[43] M. Rakotondrabe, C. Clévy, P. Lutz. IEEE Trans. Control Syst. Technol., **7** (3), 440 (2010). DOI: 10.1109/TASE.2009.2028617

[44] S.G. Alcock, I.-T. Nistea, V.G. Badami, R. Signorato, K. Sawhney. Rev. Sci. Instrum., **90** (2), 021712 (2019). DOI: 10.1063/1.5060737

[45] J.D. French, R.B. Cass. Am. Ceram. Soc. Bull., **77** (5), 61 (1998).

[46] L.J. Nelson, C.R. Bowen. Key. Eng. Mater., **206**–**213**, 1509 (2002). DOI: 10.4028/www.scientific.net/KEM.206-213.1509

[47] C.R. Bowen, R. Stevens, L.J.N.A.C. Dent, G. Dolman, B. Su, T.W. Button, M.G. Cain, M. Stewart. Smart Mater. Struct., **15** (2), 295 (2006). DOI: 10.1088/0964-1726/15/2/008

[48] M.P. Ulmer, X. Wang, J. Cao, S. Vaynman. Proc. SPIE, **8861**, 88611R (2013). DOI: 10.1117/12.2024217

[49] M.P. Ulmer, X. Wang, P. Knapp, J.-L. Cao, Y. Cao, T. Karian, S. Grogans, M. Graham, S. Vaynman, Y. Yao. Proc. SPIE, **9208**, 920808 (2014). DOI: 10.1117/12.2062008

[50] X. Wang, Y. Yao, J. Cao, S. Vaynman, M.E. Graham, T. Liu, M.P. Ulmer. Proc. SPIE, **9603**, 96031O (2015). DOI: 10.1117/12.2187070

[51] A.K. Bastola, M. Hossain. Materials & Design, **211**, 110172 (2021). DOI: 10.1016/j.matdes.2021.110172

[52] A. Khounsary, W. Yun. Rev. Sci. Instrum., **67** (9), 3354 (1996). DOI: 10.1063/1.1147402

[53] D. Cocco, C. Hardin, D. Morton, L. Lee, M.L. Ng, L. Zhang, L. Assoufid, W. Grizolli, X. Shi, D.A. Walko, G. Cutler, K.A. Goldberg, A. Wojdyla, M. Idir, L. Huang, G. Dovillaire. Opt. Express, **28** (13), 19242 (2020). DOI: 10.1364/OE.394310

[54] L. Zhang, D. Cocco, N. Kelez, D.S. Morton, V. Srinivasan, P.M. Stefan. J. Synchrotron Rad., **22** (5), 1170 (2015). DOI: 10.1107/S1600577515013090

[55] D. Laundy, V. Dhamgaye, T. Moxham, K. Sawhney. Optica, **6** (12), 1484 (2019). DOI: 10.1364/OPTICA.6.001484

[56] B. Jenichen, R. Köhler, W. Möhling. J. Phys. E: Sci. Instrum., **21** (11), l062 (1988). DOI: 10.1088/0022-3735/21/11/012

[57] B. Jenichen, T. Wroblewski, R. Köhler. J. Phys. D: Appl. Phys., **28** (4A), A266 (1995). DOI: 10.1088/0022-3727/28/4A/052

[58] M. Popovici, W.B. Yelon. J. Appl. Cryst., **25** (4), 471 (1992). DOI: 10.1107/S0021889892000359

[59] S. Stoupin, Z. Liu, S.M. Heald, D. Brewe, M. Meron. J. Appl. Cryst., **48** (6), 1734 (2015). DOI: 10.1107/S1600576715017446

[60] F. Seiboth, A. Schropp, M. Scholz, F. Wittwer, C. Rödel, M. Wünsche, T. Ullsperger, S. Nolte, J. Rahomäki, K. Parfeniukas, S. Giakoumidis, U. Vogt, U. Wagner, C. Rau, U. Boesenberg, J. Garrevoet, G. Falkenberg, E.C. Galtier, H. Ja Lee, B. Nagler, C.G. Schroer. Nat. Commun., **8** (1), 14623 (2017). DOI: 10.1038/ncomms14623

[61] K. Sawhney, D. Laundy, V. Dhamgaye, I. Pape. Appl. Phys. Lett., **109** (5), 051904 (2016). DOI: 10.1063/1.4960593

[62] D. Laundy, V. Dhamgaye, I. Pape, K.J. Sawhney. Proc. SPIE, **10386**, 103860B (2017). DOI: 10.1117/12.2275134

[63] T. Kimura, S. Handa, H. Mimura, H. Yumoto, D. Yamakawa, S. Matsuyama, K. Inagaki, Y. Sano, K. Tamasaku, Y. Nishino, M. Yabashi, T. Ishikawa, K. Yamauchi. Jpn. J. Appl. Phys., **48** (7), 072503 (2009). DOI: 10.1143/JJAP.48.072503

[64] H. Mimura, S. Handa, T. Kimura, H. Yumoto, D. Yamakawa, H. Yokoyama, S. Matsuyama, K. Inagaki, K. Yamamura, Y. Sano, K. Tamasaku, Y. Nishino, M. Yabashi, T. Ishikawa, K. Yamauchi. Nat. Phys., **6** (2), 122 (2010). DOI: 10.1038/nphys1501

[65] K. Yamauchi, H. Mimura, T. Kimura, H. Yumoto, S. Handa, S. Matsuyama, K. Arima, Y. Sano, K. Yamamura, K. Inagaki, H. Nakamori, J. Kim, K. Tamasaku, Y. Nishino, M. Yabashi, T. Ishikawa. J. Phys.: Condens. Matter, **23** (39), 394206 (2011). DOI: 10.1088/0953-8984/23/39/394206

[66] H. Mimura, T. Kimura, H. Yokoyama, H. Yumoto, S. Matsuyama, K. Tamasaku, Y. Koumura, M. Yabashi, T. Ishikawa, K. Yamauchi. AIP Conf. Proc., **1365**, 13 (2011). DOI: 10.1063/1.3625294

[67] C.L. Hardin, V.N. Srinivasan, L. Amores, N.M. Kelez, D.S. Morton, P.M. Stefan, J. Nicolas, L. Zhang, D. Cocco. Proc. SPIE, **9965**, 996505 (2016). DOI: 10.1117/12.2235825

[68] W.N. Davis, P.B. Reid, D.A. Schwartz. Proc. SPIE, **7803**, 78030P (2010). DOI: 10.1117/12.862522

[69] K.J.S. Sawhney, S.G. Alcock, R. Signorato. Proc. SPIE, **7803**, 780303 (2010). DOI: 10.1117/12.861593

[70] P. Mercere, M. Idir, G. Dovillaire, X. Levecq, S. Bucourt, L. Escolano, P. Sauvageot. Proc. SPIE, **7803**, 780302 (2010). DOI: 10.1117/12.860990

[71] C. Svetina, D. Cocco, A. Di Cicco, C. Fava, S. Gerusina, R. Gobessi, N. Mahne, C. Masciovecchio, E. Principi, L. Raimondi, L. Rumiz, R. Sergo, G. Sostero, D. Spiga, M. Zangrando. Proc. SPIE, **8503**, 850302 (2012). DOI: 10.1117/12.929701

[72] L.A. Poyneer, N.F. Brejnholt, R. Hill, J. Jackson, L. Hagler, R. Celestre, J. Feng. Rev. Sci. Instrum., **87** (5), 052003 (2016). DOI: 10.1063/1.4950739

[73] J.P. Sutter, P.A. Chater, R. Signorato, D.S. Keeble, M.R. Hillman, M.G. Tucker, S.G. Alcock, I.-T. Nistea, H. Wilhelm. Opt. Express, **27** (11), 16121 (2019). DOI: 10.1364/OE.27.016121

[74] S.G. Alcock, J.P. Sutter, K.J.S. Sawhney, D.R. Hall, K. McAuley, T. Sorensen. Nucl. Instrum. Meth. Phys. Res. A, **710**, 87 (2013). DOI: 10.1016/j.nima.2012.10.135

[75] T. Goto, S. Matsuyama, H. Hayashi, H. Yamaguchi, J. Sonoyama, K. Akiyama, H. Nakamori, Y. Sano, Y. Kohmura, M. Yabashi, T. Ishikawa, K. Yamauchi. Opt. Express, **26** (13), 17477 (2018). DOI: 10.1364/OE.26.017477

[76] S. Matsuyama, H. Yamaguchi, T. Inoue, Y. Nishioka, J. Yamada, Y. Sano, Y. Kohmura, M. Yabashi, T. Ishikawa, K. Yamauchi. Opt. Express, **29** (10), 15604 (2021). DOI: 10.1364/OE.422723

[77] P. Kirkpatric, A.V. Baez. J. Opt. Soc. Am. **38** (9), 766 (1948). DOI: 10.1364/JOSA.38.000766

[78] M. Cianci, G. Bourenkov, G. Pompidor, I. Karpics, J. Kallio, I. Bento, M. Roessle, F. Cipriani, S. Fiedler, T.R. Schneider. J. Synchrotron Rad., **24** (1), 323 (2017). DOI: 10.1107/S1600577516016465

[79] T. Kimura, S. Matsuyama, K. Yamauchi, Y. Nishino. Opt. Express, **21** (8), 9267 (2013). DOI: 10.1364/OE.21.009267

[80] K.P. Singh. J. Opt., **40** (3) 88 (2011). DOI: 10.1007/s12596-011-0040-2

[81] A.-C. Probst, T. Döhring, M. Stollenwerk, M. Wen, L. Proserpio. Proc. SPIE, **10562**, 105621E (2016). DOI: 10.1117/12.2296167

[82] E. Wille, M. Bavdaz. Acta Astronautica, **116** (9), 50 (2015). DOI: 10.1016/j.actaastro.2015.06.011

[83] R. Petre. X-ray Opt. Instru., **2010** (8), ID 412323 (2010). DOI: 10.1155/2010/412323

[84] A. Winter, E. Breunig, P. Friedrich, L. Proserpio. Proc. SPIE, **10563**, 1056321 (2017). DOI: 10.1117/12.2304243

[85] V. Cotroneo, R. Allured, C.T. DeRoo, K.L. Gurski, V. Marquez, P.B. Reid, E.D. Schwartz. Proc. SPIE, **10399**, 10399 (2017). DOI: 10.1117/12.2275738

[86] V. Navalkar, K.P. Singh, M. J. Press. Astrophys. Astron., **40** (3), 24 (2019). DOI: 10.1007/s12036-019-9592-3

[87] S.L. O'Dell, T.L. Aldcroft, C. Atkins, T.W. Button, V. Cotroneo, W.N. Davis, P. Doel, C.H. Feldman, M.D. Freeman, M.V. Gubarev, R.L. Johnson-Wilke, J.J. Kolodziejczak, C.F. Lillie, A.G. Michette, B.D. Ramsey, P.B. Reid, D. Rodriguez Sanmartin, T.T. Saha, D.A. Schwartz, S.E. Trolier-McKinstry, M.P. Ulmer, R.H.T. Wilke, R. Willingale, W.W. Zhang. Proc. SPIE., **8503**, 850307 (2012). DOI: 10.1117/12.930090

[88] P.B. Reid, S.S. Murray, S. Trolier-McKinstry, M. Freeman, M. Juda, W. Podgorski, B. Ramsey, D. Schwartz. Proc. SPIE, **7011**, 70110V (2008). DOI: 10.1117/12.789371

[89] W.W. Craig, C.J. Hailey, M. Jimenez-Garate, D.L. Windt. Opt. Express, **7** (4), 178 (2000). DOI: 10.1364/OE.7.000178

[90] M. Elvis, R.J. Brissenden, G. Fabbiano, D.A. Schwartz, P. Reid, W. Podgorski, M. Eisenhower, M. Juda, J. Phillips, L. Cohen, S. Wolk. Proc. SPIE, **6266**, 62661K (2006). DOI: 10.1117/12.672072

[91] C. Feldman, R. Willingale, C. Atkins, H. Wang, P. Doel, D. Brooks, S. Thompson, T. Button, D. Zhang, D. Rodriguez Sanmartin, A. James, C. Theobald. Proc. SPIE, **7011**, 70110Y (2008). DOI: 10.1117/12.788759

[92] P.B. Reid, T.L. Aldcroft, V. Cotroneo, W. Davis, R. Johnson-Wilke, L. McMuldroch, B.D. Ramsey, D.A. Schwartz, S. Trolier-McKinstry, A. Vikhlinin, H. Rudeger S., R.H.T. Wilke. Proc. SPIE, **8443**, 84430T (2012). DOI: 10.1117/12.926930

[93] D. Spiga, M. Barbera, A. Collura, S. Basso, R. Candia, M. Civitani, M.S. Di Bella, G. Di Cicca, U. Lo Cicero, G. Lullo, C. Pelliciari, M. Riva, B. Salmaso, L. Sciortino, S. Varisco. J. Synchrotron Rad., **23** (1), 59 (2016). DOI: 10.1107/S1600577515017142

[94] C.T. DeRoo, R. Allured, V. Cotroneo, E.N. Hertz, V. Marquez, P.B. Reid, E.D. Schwartz, A.A. Vikhlinin, S. Trolier-McKinstry, J. Walker, T.N. Jackson, T. Liu, M. Tendulkar. J. Astron. Telesc. Instrum. Syst., **4** (1), 019004 (2018). DOI: 10.1117/1.JATIS.4.1.019004

[95] J. Walker, T. Liu, M. Tendulkar, D.N. Burrows, C.T. DeRoo, R. Allured, E.N. Hertz, V. Cotroneo, P.B. Reid, E.D. Schwartz, T.N. Jackson, S. Trolier-McKinstry. Opt. Express, **26** (21), 27757 (2018). DOI: 10.1364/OE.26.027757

[96] W.W. Zhang, K.D. Allgood, M.P. Biskach, K.-W. Chan, M. Hlinka, J.D. Kearney, J.R. Mazzarella, R.S. McClelland, Ai Numata, R.E. Riveros, T.T. Saha, P.M. Solly. Proc. SPIE, **11119**, 1111907 (2019). DOI: 10.1117/12.2530284

[97] M.C. Weisskopf, J. Gaskin, H. Tananbaum, A. Vikhlinin. Proc. SPIE, **9510**, 951002 (2015). DOI: 10.1117/12.2185084

[98] J.M. Roche, R.F. Elsner, B.D. Ramsey, S.L. O'Dell, J.J. Kolodziejczak, M.C. Weisskopf, M.V. Gubarev. Proc. SPIE, **9965**, 99650I (2016). DOI: 10.1117/12.2238171

[99] D.A. Schwartz, R. Allured, J.A. Bookbinder, V. Cotroneo, W.R. Forman, M.D. Freeman, S. McMuldroch, P.B. Reid, H. Tananbaum, A.A. Vikhlinin, R.L. Johnson-Wilke, S.E. Trolier-McKinstry, R.H.T. Wilke, T.N. Jackson, J. Israel Ramirez, M.V. Gubarev, J.J. Kolodziejczak, S.L. O'Dell, B.D. Ramsey. Proc. SPIE, **9208**, 920806 (2014). DOI: 10.1117/12.2063469.

[100] R.L. Johnson-Wilke, R.H.T. Wilke, M.L. Wallace, J.I. Ramirez, Z. Prieskorn, J. Nikoleyczik, V. Cotroneo, R. Allured, D.A. Schwartz, S. McMuldroch, P.B. Reid, D.N. Burrows, T.N. Jackson, S. Trolier-McKinstry. Proc. SPIE, **9208**, 920809 (2014). DOI: 10.1117/12.2063369

[101] H. Wang, J. Sutter, K. Sawhney. Opt. Express, 23(2), 1605 (2015). DOI: 10.1364/OE.23.001605

[102] H. Wang, K. Sawhney, S. Berujon, J. Sutter, S.G. Alcock, U. Wagner, C. Rau. Opt. Lett., **39** (8), 2518 (2014). DOI: 10.1364/OL.39.002518

[103] H. Wang, S. Berujon, J. Sutter, S.G. Alcock, K. Sawhney. Proc. SPIE, **9206**, 920608 (2014). DOI: 10.1117/12.2062828

[104] D. Cocco, M. Idir, D. Morton, L. Raimondi, M. Zangrando. Nucl. Instrum. Methods Phys. Res. A, **907**, 105 (2018). DOI: 10.1016/j.nima.2018.03.026

[105] O. Soloviev, G. Vdovin. Opt. Express, **13** (23), 9570 (2005). DOI: 10.1364/OPEX.13.009570

[106] A. Polo, V. Kutchoukov, F. Bociort, S.F. Pereira, H.P. Urbach. Opt. Express, **20** (7), 7822 (2012). DOI: 10.1364/OE.20.007822

[107] M. Rais, J.-M. Morel, C. Thiebaut, J.-M. Delvit, G. Facciolo. Appl. Opt., **55** (28) 7836 (2016). DOI: 10.1364/AO.55.007836

[108] M. Aftab, H. Choi, R. Liang, D. Wook Kim. Opt. Express, **26** (26), 34428 (2018). DOI: 10.1364/OE.26.034428

[109] J. Susini, G. Marot, L. Zhang. Rev. Sci. Instrum., **63** (1), 489 (1992). DOI: 10.1063/1.1142740

[110] O. de La Rochefoucauld, G. Dovillaire, F. Harms, M. Idir, L. Huang, X. Levecq, M. Piponnier, P. Zeitoun. Sensors, **21** (3), 874 (2021). DOI: 10.3390/s21030874

[111] B.C. Platt, R. Shack. J. Refract. Surg., **17** (5), S573 (2001). DOI: 10.3928/1081-597X-20010901-13

[112] K.L. Baker, J. Brase, M. Kartz, S.S. Olivier, B. Sawvel, J. Tucker. Opt. Lett., **28** (3), 149 (2003). DOI: 10.1364/ol.28.000149

[113] S.C. Mayo, B. Sexton. Opt. Lett., **29** (8), 866 (2004). DOI: 10.1364/ol.29.000866

[114] S. Reich, T. dos Santos Rolo, A. Letzel, T. Baumbach, A. Plech. Appl. Phys. Lett., **112**, 151903 (2018). DOI: 10.1063/1.5022748

[115] H.F. Talbot. Phil. Mag. **9**, 401 (1836).

[116] K. Banaszek, K. Wodkiewicz, W.P. Schleich. Opt. Express., **2** (5), 169 (1998). DOI: 10.1364/OE.2.000169

[117] T. Weitkamp, C. David, C. Kottler, O. Bunk, F. Pfeiffer. Proc. SPIE, **6318**, 63180S (2006). DOI: 10.1117/12.683851

[118] Y. Kayser, C. David, U. Flechsig, J. Krempasky, V. Schlott, R. Abela. J. Synchrotron Rad., **24** (1), 150 (2017). DOI: 10.1107/S1600577516017562

[119] T. Weitkamp, B. Nöhammer, A. Diaz, C. David, E. Ziegler. Appl. Phys. Lett., **86** (5), 054101 (2005). DOI: 10.1063/1.1857066

[120] A. Diaz, C. Mocuta, J. Stangl, M. Keplinger, T. Weitkamp, F. Pfeiffer, C. David, T.H. Metzger, G. Bauer. J. Synchrotron. Radiat., **17** (3), 299 (2010). DOI: 10.1107/S0909049510004644

[121] H. Wang, K. Sawhney, S. Berujon, E. Ziegler, S. Rutishauser, C. David. Opt. Express, **19** (17), 16550 (2011). DOI: 10.1364/OE.19.016550

[122] S. Rutishauser, L. Samoylova, J. Krzywinski, O. Bunk, J. Grunert, H. Sinn, M. Cammarata, D.M. Fritz, C. David. Nat. Commun., **3** (1), 947 (2012). DOI: 10.1038/ncomms1950

[123] W. Grizolli, X. Shi, L. Assoufid, L.G. Butler. AIP Conf. Proc., **2054** (1), 060017 (2019). DOI: 10.1063/1.5084648

[124] S. Zhao, Y. Yang, Y. Shen, G. Cheng, Y. Wang, Q. Wang, L. Zhang, K. Wang. Opt. Express, **29** (14), 22704 (2021). DOI: 10.1364/OE.430269

[125] M. Takeda, H. Ina, S Kobayashi. J. Opt. Soc. Am., **72** (1), 156 (1982). DOI: 10.1364/JOSA.72.000156

[126] T. Weitkamp, A. Diaz, B. Nöhammer, F. Pfeiffer, M. Stampanoni, E. Ziegler, C. David. Proc. SPIE, **5533**, 140 (2004). DOI: 10.1117/12.559695

[127] S. Yuan, K. Goldberg, V.V. Yashchuk, R. Celestre, W.R. McKinney, G. Morrison, J. Macdougall, I. Mochi, T. Warwick. Nucl. Instrum. Methods Phys. Res. A, **635** (1), S58 (2011). DOI: 10.1016/J.NIMA.2010.09.120

[128] I. Zanette, T. Weitkamp, T. Donath, S. Rutishauser, Ch. David. Phys. Rev. Lett., **105** (24), 248102 (2010). DOI: 10.1103/PHYSREVLETT.105.248102

[129] S. Rutishauser, I. Zanette, T. Weitkamp, T. Donath, C. David. Appl. Phys. Lett., **99** (22), 221104 (2011). DOI: 10.1063/1.3665063

[130] S. Berujon, E. Ziegler. Opt. Lett., **37** (21), 4464 (2012). DOI: 10.1364/OL.37.004464

[131] S. Matsuyama, H. Yokoyama, R. Fukui, Y. Kohmura, K. Tamasaku, M. Yabashi, W. Yashiro, A. Momose, T. Ishikawa, K. Yamauchi. Opt. Express, **20** (22), 24977 (2012). DOI: 10.1364/OE.20.024977

[132] D.J. Merthe, K.A. Goldberg, V.V. Yashchuk, W.R. McKinney, R. Celestre, I. Mochi, J. MacDougall, G.Y. Morrison, S.B. Rekawa, E. Anderson, B.V. Smith, E.E. Domning,

H. Padmore. Nucl. Instrum. Methods Phys. Res. A, **710**, 82 (2013). DOI: 10.1016/j.nima.2012.10.105

[133] S. Marathe, X. Shi, A.M. Khounsary, M.J. Wojcik, N.G. Kujala, A.T. Macrander, L. Assoufid. Proc. SPIE, **9208**, 92050D (2014). DOI: 10.1117/12.2062460

[134] K. Yamauchi, M. Yabashi, H. Ohashi, T. Koyamac, T. Ishikawa. J. Synchrotron Rad., **22** (3), 592 (2015). DOI: 10.1107/S1600577515005093

[135] M. Giglio, D. Brogioli, M.A.C. Potenza, A. Vailati. Phys. Chem. Chem. Phys., **6** (7), 1547 (2004). DOI: 10.1039/b314600f

[136] S. Berujon, E. Ziegler, R. Cerbino, L. Peverini. Phys. Rev. Lett., **108** (15), 158102 (2012). DOI: 10.1103/PhysRevLett.108.158102

[137] R. Cerbino, L. Peverini, M.A.C. Potenza, A. Robert, P. Bösecke, M. Giglio. Nat. Phys., **4** (3), 238 (2008). DOI: 10.1038/nphys837

[138] S. Berujon, H. Wang, K.J.S. Sawhney. J. Physics: Conf. Series, **425** (5), 052020 (2013). DOI: 10.1088/1742-6596/425/5/052020

[139] K. Sawhney, S. Alcock, J. Sutter, S. Berujon, H. Wang, R. Signorato. J. Physics: Conf. Series, **425** (5), 052026 (2013). DOI: 10.1088/1742-6596/425/5/052026

[140] S. Berujon, H. Wang, S. Alcock, K. Sawhney. Opt. Express, **22** (6), 6438 (2014). DOI: 10.1364/OE.22.006438

[141] H. Wang, Y. Kashyap, K. Sawhney. Opt. Express, **23** (18), 23310 (2015). DOI: 10.1364/OE.23.023310

[142] Y. Kashyap, H. Wang, K. Sawhney. Rev. Sci. Instrum., **87** (5), 052001 (2016). DOI: 10.1063/1.4949004

[143] H. Wang, T. Zhou, Y. Kashyap, K. Sawhney. Proc. SPIE, **10388**, 103880I (2017). DOI: 10.1117/12.2274781

[144] L. Xue, H. Luo, Q. Diao, F. Yang, J. Wang, Z. Li. Sensors, **20** (22), 6660 (2020). DOI: 10.3390/s20226660

[145] S. Berujon, R. Cojocaru, P. Piault, R. Celestre, T. Roth, R. Barrett, E. Ziegler. J. Synchrotron Rad., **27** (2), 284 (2020). DOI: 10.1107/S1600577520000491

[146] B. Pan, K. Qian, H. Xie, A. Asundi. Meas. Sci. Technol., **20** (6), 062001 (2009). DOI: 10.1088/0957-0233/20/6/062001

[147] S. Berujon, H. Wang, I. Pape, K. Sawhney. Appl. Phys. Lett., **102** (15), 154105 (2013). DOI: 10.1063/1.4802729

[148] C. Kottler, C. David, F. Pfeiffer, O. Bunk. Opt. Express, **15** (3), 1175 (2007). DOI: 10.1364/oe.15.001175

[149] Y. Kashyap, Wang H., K. Sawhney. J. Synchrotron Rad., **23** (5), 1131 (2016). DOI: 10.1107/S1600577516012509

[150] T. Zhou, H. Wang, O. Fox, K. Sawhney. Opt. Express, **26** (21), 26961 (2018). DOI: 10.1364/OE.26.026961

[151] W.H. Southwell. J. Opt. Soc. Am., **70** (8), 998 (1980). DOI: 10.1364/JOSA.70.000998

[152] R.T. Frankot, R. Chellappa. IEEE Trans. Pattern Anal. Machine Intell. **10** (4), 439 (1988). DOI: 10.1109/34.3909

[153] S. Berujon, R. Cojocaru, P. Piault, R. Celestre, T. Roth, R. Barrett, E. Ziegler. J. Synchrotron Rad., **27** (2), 293 (2020). DOI: 10.1107/S1600577520000508

[154] F. Pfeiffer. Nat. Photonics, **12** (1), 9 (2018). DOI: 10.1038/s41566-017-0072-5

[155] A. Schropp, P. Boye, J.M. Feldkamp, R. Hoppe, J. Patommel, D. Samberg, S. Stephan, K. Giewekemeyer, R.N. Wilke, T. Salditt, J. Gulden, A.P. Mancuso, I.A. Vartanyants, E. Weckert, S. Schöder, M. Burghammer, C.G. Schroer. Appl. Phys. Lett., **96** (9), 091102 (2010). DOI: 10.1063/1.3332591

[156] C.M. Kewish, P. Thibault, M. Dierolf, O. Bunk, A. Menzel, J. Vila-Comamala, K. Jefimovs, F. Pfeiffer. Ultramicroscopy, **110** (4), 325 (2010). DOI: 10.1016/j.ultramic.2010.01.004

[157] S. Hoenig, R. Hoppe, J. Patommel, A. Schropp, S. Stephan, S. Schöder, M. Burghammer, C.G. Schroer. Opt. Express, **19** (17), 16324 (2011). DOI: 10.1364/OE.19.016324

[158] P. Thibault, M. Dierolf, A. Menzel, O Bunk., C. David, F. Pfeiffer. Science, **321** (5887), 379 (2008). DOI: 10.1126/science.1158573

[159] P. Thibault, M. Dierolf, O. Bunk, A. Menzel, F. Pfeiffer. Ultramicroscopy, **109** (4), 338 (2009). DOI: 10.1016/j.ultramic.2008.12.011

[160] A.M. Maiden, J.M. Rodenburg. Ultramicroscopy, **109** (10), 1256 (2009). DOI: 10.1016/j.ultramic.2009.05.012

[161] E.T.B. Skjønsfjell, Y. Chushkin, F. Zontone, N. Patil, A. Gibaud, D.W. Breiby. Opt. Express, **24** (10), 10710 (2016). DOI: 10.1364/OE.24.010710

[162] K. Sawhney, H. Wang, J. Sutter, S. Alcock, S. Berujon. Synchrotron Rad. News, **26** (5), 17 (2013). DOI: 10.1080/08940886.2013.832586

[163] M. Idir, P. Mercere, M.H. Modi, G. Dovillaire, X. Levecq, S. Bucourt, L. Escolano, P. Sauvageot. Nucl. Instrum. Methods Phys. Res. A, **616** (2–3), 162 (2010). DOI: 10.1016/j.nima.2009.10.168

[164] J. Susini, R. Baker, M. Krumrey, W. Schwegle, A. Kvick. Rev. Sci. Instrum., **66** (2), 2048 (1995). DOI: 10.1063/1.1145725

[165] E. Abruña, V.G. Badami, L. Huang, M. Idir. Proc. SPIE, **10761**, 107610H (2018). DOI: 10.1117/12.2323698

[166] V.G. Badami, E. Abruña, L. Huang, M. Idir. Rev. Sci. Instrum., **90** (2), 021703 (2019). DOI: 10.1063/1.5060954

[167] A.G. Poleshchuk, V.N. Khomutov, A.E. Matochkin, R.K. Nasyrov, V.V. Cherkashin. Photonics, (4), 38 (2016). DOI: 10.22184/1993-7296.2016.58.4.38.50

[168] F. Zamkotsian, P. Lanzoni, R. Barette, M. Helmbrecht, F. Marchis, A. Teichman. Micromachines, **8** (8), 233 (2017). DOI: 10.3390/mi8080233

[169] W. Grizolli, X. Shi, T. Kolodziej, Y. Shvyd'ko, L. Assoufid. Proc. SPIE, **10385**, 1038502 (2017). DOI: 10.1117/12.2274023

[170] S.P. Kearney, L. Assoufid, W. Grizolli, T. Kolodziej, K. Lang, A. Macrander. Proc. MEDSI 2018 Conference, 394 (2018). DOI: 10.18429/JACoW-MEDSI2018-THPH27

[171] K.A. Goldberg, A. Wojdyla, D. Bryant, W. Chao, D. Cocco, C. Hardin, D. Morton, M.L. Ng, L. Lee, L. Assoufid, W. Grizolli, X. Shi, S.P. Kearney, M. Wojcik, Y. Shvyd'ko, D. Shu, M. Idir, L. Huang. Proc. SPIE, **11109**, 111090C (2019). DOI: 10.1117/12.2530817

[172] S. Duan, J. Wu, J. Xia, W. Lei. Sensors, **20** (10), 2820 (2020). DOI: 10.3390/s20102820O65-22